Solid micellar Ru single-atom catalysts for the water-free hydrogenation of CO2 to formic acid

Qiyan Wang, Sara Santos, César Urbina-Blanco, Willinton Hernández, Marianne Impéror-Clerc, Evgeny Vovk, Maya Marinova, Ovidiu Ersen, Walid Baaziz, Olga Safonova, et al.

Solid micellar Ru single-atom catalysts for the water-free hydrogenation of CO_2 to formic acid

Qiyan Wang,[a,b] Sara Santos,[c,#] César A. Urbina-Blanco,[c] Willinton Y. Hernández,[a] Marianne Impéror-Clerc,[d] Evgeny I. Vovk,[e] Maya Marinova,[f] Ovidiu Ersen,[g] Walid Baaziz,[g] Olga V. Safonova,[h] Andrei Y. Khodakov,[b] Mark Saeys,[c]* Vitaly V. Ordomsky*

[a, b]*

[a] *Eco-Efficient Products and Processes Laboratory (E2P2L), UMI 3464 CNRS-Solvay, 201108 Shanghai, People's Republic of China;*

[b] *Univ. Lille, CNRS, Centrale Lille, ENSCL, Univ. Artois, UMR 8181 – UCCS – Unité de Catalyse et Chimie du Solide, F-59000 Lille, France;*

[c] *Laboratory for Chemical Technology (LCT), Department of Materials, Textiles and Chemical Engineering, Ghent University, Technologiepark 125, 9052 Ghent, Belgium.*

[d] *Laboratoire de Physique de Solides, CNRS, Université Paris-Sud, Université Paris-Saclay, 91400 Orsay, France;*

[e] *School of Physical Science and Technology, Shanghai Tech University, Shanghai 201210, People's Republic of China;*

[f] *Institut Chevreul, FR2638 CNRS, Bât. C6 Université Lille 1, F-59655 Villeneuve d'Ascq, France*

[g] *IPCMS, UMR 7504 CNRS, Université de Strasbourg, 23 rue du Loess, BP 43-67034 Strasbourg Cedex 2, France;*

[h] *Paul Scherrer Institute, CH-5232 Villigen, Switzerland*

[#] *equal contribution*

ABSTRACT. The catalytic hydrogenation of CO_2 to formic acid is one of the most promising pathways towards a renewable hydrogen-storage system. The reaction is usually performed in aqueous phase in the presence of basic molecules over homogeneous or heterogeneous catalysts, generating relatively dilute formate solutions (<1 M).

The newly designed solid micellar Ru single-atom catalyst enables efficient and stable water-free CO_2 hydrogenation to formate under mild reaction conditions. Concentrated formate solutions (up to 4 M) are produced directly from the hydrogenation of carbon dioxide in water-free tertiary amine. In the catalyst, Ru(III) single sites are incorporated into the walls of MCM-41 during hydrolysis creating a solid micelle structure. The presence of the CTA^+ surfactant in the pores of MCM-41 stabilizes the Ru sites and prevents catalyst deactivation. DFT modelling suggests that the reaction proceeds via heterolytic hydrogen splitting, forming a Ru-H species and subsequent hydride transfer to CO_2.

KEYWORDS. Ru, solid micelles, single-atom catalysts, CO_2 hydrogenation, formic acid.

1. Introduction

The catalytic hydrogenation of CO_2 has attracted much attention in recent years because it not only serves to mitigate the problem of anthropogenic CO_2 emissions but also provides a feasible avenue for carbon recycling and hydrogen energy conversion and storage [1-2]. Among the various hydrogenation products of CO_2, formic acid is one of the most attractive, owing to its direct employment as a feedstock chemical and as a hydrogen source for fuel cells [3-4]. In addition, the conversion of CO_2 to formic acid is believed to be the first and indispensable step in the reduction of CO_2 to other chemicals or fuels, such as formaldehyde, methanol, methane, or other hydrocarbons. A fundamental understanding of this reaction is essential for C_1 chemistry [5-7].

CO_2 conversion is often challenging, owing to the thermodynamic stability of this molecule [7]. Unfavorable thermodynamics requires the presence of bases like tertiary amines, alkali hydroxides or carbonates in order to shift the equilibrium of the reaction toward stable formate [8-9]. High CO_2 conversions have been accomplished using homogeneous catalysts containing electron-donating ligands on the active metal centers [10]. For example, high efficiency has been achieved using ruthenium phosphine [11], pincer [12] and amine complexes [13]. Heterogeneous catalysts provide significant advantages related to stability and recyclability, rending them technologically advantageous and the preferred industrial choice [14]. An attempt was made recently to prepare efficient CO_2 hydrogenation catalysts via immobilization of Ru cations on rather sophisticated bipyridine-functionalized covalent triazine framework [15].

Homogeneous Ru-based catalysts have been used for CO_2 hydrogenation in water-free conditions in organic solvents like DMSO [16], THF [17], diglyme[18] etc., but water-free heterogeneous CO_2 hydrogenation to formic acid has not been reported since high concentrations of strong bases are detrimental to the activity and stability of heterogeneous catalysts [19]. Water is also often involved in the reaction mechanism via the formation of carbonate species in the equilibrium $CO_2/H_2CO_3/HCO_3^-$, with hydrogen transfer for the synthesis of formate [14]. However, the presence of water necessitates an energy-intensive distillation step to produce concentrated formic acid [20], thereby reducing the potential benefit of CO_2 hydrogenation over the conventional route [21].

Supported single-atom catalysts (SACs) have found numerous applications in selective chemical synthesis. They consist of isolated individual atoms dispersed on, and/or coordinated with a support [22]. This term was first coined by Zhang *et al.* in 2011[23], when reporting on the discovery of a new Pt_1/FeO_x material for CO oxidation. SACs have a dual advantage of nearly 100 % atomic utilization, similar to homogeneous catalysts, as well as easy separation from the reaction media due to their heterogeneous supported nature [24]. The concept of SAC in comparison with grafted homogeneous catalyst implies use of inorganic supports as a rigid ligand. Recently, a new type of SAC catalysts has been proposed, which contain also organic ligands in the structure to tune the charge of metal atoms and stabilize them [25].

In this paper, we propose a new Ru single-atom catalyst elaborated using a modified MCM-41 with cetyltrimethylammonium (CTA) as the template and $RuCl_3$ as the metal precursor (**Figure 1**). The use of solid micelle concept allows us providing high content of Ru in the material with uniform distribution of the active sites. The newly developed catalyst is prepared by the hydrolysis of $RuCl_3$ under basic conditions, resulting in the incorporation of single Ru atoms into the walls of MCM-41, stabilized by the CTA^+ surfactant. This new catalytic material combines the advantages of homogeneous and heterogeneous catalysts for the selective synthesis of formate from carbon dioxide. On the one hand, it allows conducting the reaction without deactivation in the presence of strong bases in aqueous solution and obtaining highly concentrated formate solutions (4 M). On the other hand, easy separation of the catalyst and reaction products can be achieved.

2. Materials and methods

2.1 Preparation of catalysts

The catalysts have been prepared using a modified procedure for the synthesis of MCM-41 with addition of $RuCl_3$ at the initial step (**Figure 1**)[26].

The catalyst preparation details are given in here. 0.5 g CTAB was added to 96 mL of deionized H_2O together with 34 ml of ethanol under stirring. Afterwards, 0.09 g $RuCl_3$ (to provide the ratio CTAB/Ru=3) was added to the mixture and stirred about 10 min. After the solution turned clear, 10 mL of aqueous ammonia solution with 2 mL of TEOS was poured into the $RuCl_3$/CTAB solution with continuous stirring for 3 h at room temperature. The solid product was recovered by filtration, washed in water

and dried at room temperature overnight. The synthesized sample was denoted as **Ru@MCM-3**. **Ru@MCM-1** and **Ru@MCM-5** have been synthesized by adjusting the ratio of CTAB/Ru equal to 1 and 5, respectively. **Ru@MCM-3-used** is a catalyst after 4 catalytic cycles. **MCM-41** has been prepared in the same way but without addition of $RuCl_3$ and subsequent calcination at 550 ºC for 4 h.

The sample **Ru@MCM-3-NH_4^+** has been prepared by subsequent ion exchange of CTA^+ by NH_4^+ in Ru@MCM-3. 200 mg Ru@MCM-3 mixed with saturated ammonium chloride solution in ethanol (NH_4Cl/ethanol: 1/50, wt) has been refluxed at 80 °C for 2h with subsequent catalyst separation and washing with ethanol. The procedure has been repeated for 3 times and dried afterwards at 80 ºC.

Ru/MCM has been prepared by RuCl3 impregnation over MCM-41, drying at 80 ºC and calcination at 550 ºC for 4 h. The catalyst was reduced afterwards by H_2 at 200 oC for 30 min. **$Ru(OH)_3$** has been synthesized by hydrolysis of the $RuCl_3$ solution by addition of $NH_3 \cdot H_2O$ (25%). The calcination of $Ru(OH)_3$ at 450 °C for 2h was used for the synthesis of **RuO_2**[27].

2.2 Characterization

X-ray diffraction (XRD) was recorded on a PANalytical Empyrean X-ray diffractometer in Bragg-Brentano configuration with the 0.02° step size and 1 s step time. Cu Kα radiation (40 kV and 30 mA) was used as the X-ray source. N_2 adsorption isotherms were collected by a volumetric gas adsorption analyzer (Quantachrome Instruments Autosorb-iQ-MP-AG). Typically, 50-80 mg powder sample was loaded in a 6 mm large bulb sample cell and degassed under vacuum at

120 °C for 8 h. The BET surface area was determined using the data points in the pressure range of 0.01−0.1 P/P_0 from the N_2 adsorption isotherms at 77 K. TGA was carried out by SDT Q600 (Figure 2-5) in the temperature range of 25~900 ℃ under air/N_2 conditions. Quantitative elemental analyses were performed by inductively coupled plasma optical emission spectroscopy 720-ES ICP-OES (Agilent) with axially viewing and simultaneous CCD detection. The TEM (Transmission Electron Microscopy) analyses were carried out on a Jeol 2100F (field emission gun) microscope operating at 200 kV equipped with a probe corrector for the spherical aberrations. High angle annular dark field (HAADF)-scanning transmission electron microscopy (STEM) imaging, and energy dispersive X-ray spectroscopy (EDX) of the calcined analysis were performed on a double corrected CFEG Jeol-ARM200 transmission electron microscope, operated at 200 kV and by using scanning speed 20 μs/px for imaging and 0.05 μs/px for EDX for a with a 0.1 nm probe size and a current of 120 pA. XPS analysis has been performed in a ThermoFischer ESCALAB 250Xi photoelectron spectrometer using monochromated X-ray irradiation Al Kα (hv = 1486.7 eV) and 180° double focusing hemispherical analyzer with a six-channel detector. The BE (binding energy) of the photoemission spectra was calibrated to the Si 2p peak with BE 103.4 eV for Si containing samples and to adventitious carbon C 1s peak with BE 284.8 eV. Small Angle Scattering experiments were done on two homebuilt instruments at the LPS (Laboratoire de Physique des Solides, Orsay, France). Solid materials were recorded on a SAXS instrument operating with a copper rotating anode X-ray source (CuKα = 0.1542 nm) when the micellar solutions were

recorded on a second instrument called MODIX operating with a molybdenum rotating anode X-ray source (MoKα = 0.071 nm). Data reduction from 2D-image to the radially averaged intensity was done following standard procedures using the NIKA macros written for IgorPro (Wavemetrics, Oswego, USA) [28]. The CO_2 pulse adsorption was performed using a AutoChem II 2920 apparatus from Micromeritics. 40 mg of sample was put in a quartz reactor, and the samples were purged in a flow of Ar (60 ml/min) with a heating rate of 10 ºC/min at 90 ºC for 10 min. After cooling to 45 ºC, the catalyst has been treated by CO_2 pulses in He flow until saturation. The XAS experiments at the Ru K edge were performed at the Super XAS beamline of the Swiss Light Source (PSI, Villigen, Switzerland). The incident photon beam was selected by a Si (111) channel-cut monochromator from the polychromatic beam coming from 2.9 T superbend magnet. The rejection of higher harmonics and collimation were achieved by a platinum-coated collimating mirror at 2.5 mrad located before the monochromator, while focusing was achieved by a platinum-coated torroidal mirror at 2.5 mrad. The beam energy was calibrated using metallic Ru (K edge at 22117 eV). Samples were mixed with cellulose and measured in transmission mode using 15 cm long ionization chambers filled with 1 bar of Ar and 1 bar of N_2. The size of the X-ray beam on the sample was about 1.5 mm in horizontal and 0.5 mm in vertical directions. We analyzed the EXAFS spectra using the Demeter software package and fitted Fourier transformed k^3 weighted signal for k = 3-14 $Å^{-1}$ with dk = 1 and R = 1-4 Å with dR = 0.5. Amplitude reduction factor $S_0^2 = 0.81$ was

fitted using metallic Ru reference [29]. **Table S1, SI** summarizes the EXAFS analysis results.

DFT Calculations: the adopted cluster consists of 11 Si, 19 O, 11 H and one Ru atom. The bottom part of the cluster was frozen during the calculations. Geometries and frequencies were computed at the PBE1PBE/Def2-SVP level of theory employing D3(BJ) dispersion corrections. Standard optimization and convergence criteria were used. Single-point energy calculations were performed with the larger def2-TZVP basis set. Frequency calculations confirmed the local minima. Transition states have a single imaginary frequency and were confirmed by intrinsic reaction coordinate (IRC) calculations.

2.3 General procedure for hydrogenation reactions

CO_2 hydrogenation was conducted in a 40 ml stainless-steel autoclave equipped with a magnetic stirrer, pressure gauge and an automatic temperature controller. In a typical experiment, 6 g of water or no water, 0.9 g of triethylamine (TEA) and 10 mg of catalyst were loaded into reactor. Afterwards, the reactor was sealed and pressurized by H_2 and CO_2, followed by heating to the target temperature with continuous magnetic stirring. After the reaction, the autoclave was cooled, the pressure released and the solution separated by filtration and analyzed by ^1H NMR using signals of TEA and water as internal standards.

3. Results and discussion

3.1 Synthesis of the composite material

The synthesis of MCM-41 is based on a 'cooperative self-assembly' mechanism, which implies a micellar aqueous solution, with the micelles consisting of long-chain quaternary ammonium salts, for example, cetyltrimethylammonium bromide (CTAB) (**Figure 1**) [30]. Subsequent hydrolysis of tetraethyl orthosilicate (TEOS) leads to the precipitation of a hybrid phase with a 2D hexagonal structure, containing inorganic silica walls in-between surfactant cylindrical micelles. The template can be removed by calcination or extraction [31].

In the presence of metal salts, long-chain quaternary ammonium surfactants form ionic adducts [32]. Small angle X-ray scattering (SAXS) was used to estimate the size of the micelles formed in the CTAB-ethanol-water solutions. X-ray scattering profiles for solutions containing $RuCl_3$, CTAB, and CTAB with $RuCl_3$ at different temperatures are shown in **Figure S1, SI**. As expected, CTAB and CTAB-Ru solutions both give a typical micellar signal, linked to the size and to the spatial arrangement of the micelles. A significant difference in the overall shape of the scattering curves and in the position of the structure factor peak is observed. The size of the micelles estimated from the position of the structure factor peak is 7 nm for CTAB and 6.3 nm for CTAB-Ru. These differences in the scattering curves show that the presence of the Ru salt modifies the micelles, as expected by the complexation of $RuCl_3Br^-$ by CTA^+ cations (**Figure 1**).

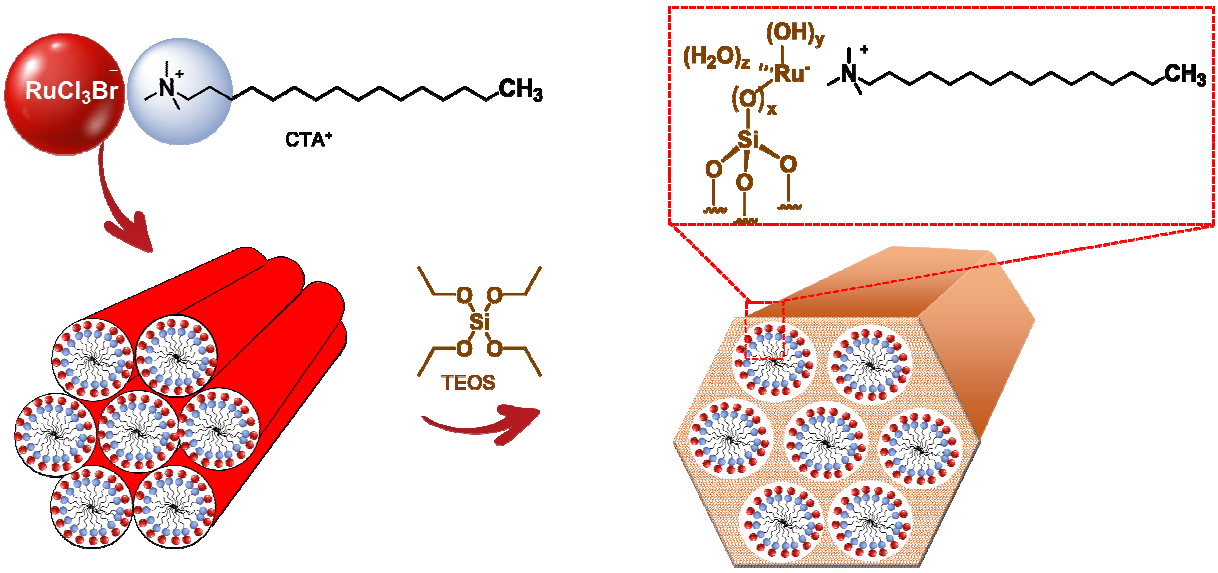

Figure 1. *Scheme of the synthesis of Ru@MCM catalyst*

Subsequent addition of TEOS leads to the synthesis of a solid material, which was studied by different physico-chemical methods. Chemical analysis confirmed the presence of Ru in the amounts corresponding to the theoretical loading in the initial composition, in the range from 3 to 15 wt. % (**Table 1**). As measured by TG analysis, the surfactant CTA contributes about 35 wt. % to the mass of the Ru@MCM-3 catalyst (**Figure S2, SI**). XPS analysis showed only trace amounts of Cl^- and Br^- in the material, indicating complete hydrolysis of $RuCl_3$ with the formation of Ru-OH or Ru-O-Si species (**Figure S3, SI**).

SAXS analysis shows the formation of a 2D hexagonal phase typical for the MCM-41 materials with 4 Bragg peaks at 10, 11, 20 and 21 (**Figure S4, SI**). This highly ordered structure is only observed for samples with relatively high CTAB/$RuCl_3$ ratios (CTAB/Ru=3 and 5), as shown by the narrow diffraction peaks. An increase in the $RuCl_3$ content results in a gradual decrease in the lattice parameter from 4.46 nm for MCM-41 to 4.32 and 4.22 nm for Ru@MCM-5 and Ru@MCM-3,

respectively. A decrease in the size of the micelles by complexation of CTAB with $RuCl_3$ is the most likely reason for this decrease (**Figure S1, SI**). The material prepared with a high Ru content (CTAB/Ru=1, Ru@MCM-1) shows broader Bragg peaks, indicating a less ordered material, as well as an additional broad peak, which is associated with an additional, disordered 'worm-like' phase without hexagonal packing.

N_2 adsorption-desorption isotherms are typical for MCM-41 materials, and identified as type IV in the IUPAC classification (**Figure S5, SI**). The presence of CTA in the pores significantly decreases the N_2-accessible internal volume from 1.0 to 0.1-0.15 cm^3/g (**Table 1**). Ion exchange of CTA^+ by NH_4^+ increases the accessibility of the pores of Ru@MCM-3.

Table 1. *Characterization of Ru@MCM materials*

Sample	Ru content, wt. %		BET analysis			Lattice parameter[b], nm
	Theor.	Analysis[a]	S, m^2/g	Vp, cm^3/g	D, nm	
MCM-41	-	-	1335	1.0	3.0	4.46
Ru/MCM	5	5	1102	0.66	2.7	-
Ru@MCM-5	2.5	3	-	-	-	4.32
Ru@MCM-3	4	3.2	36	0.1	-	4.22
Ru@MCM-3-used	4	3.1	53	0.14	-	-
Ru@MCM-3-NH_4^+	-	-	485	0.51	-	-
Ru@MCM-1	12	15	-	-	-	4.40

[a] analyzed by ICP; [b] calculated from (100) XRD peak.

STEM-HAADF images of Ru@MCM-3 (**Figure 2a**) show a well-defined hexagonal structure with a fairly uniform pore structure, similar to MCM-41. It is interesting to note that the Ru@MCM-3 crystalls have as "cigar-like" morphology,

with diameters of about 10-20 nm and lengths of 150-300 nm. Because of the high sensitivity to the Z atomic number, STEM-HAADF is particularly suited to assess the Ru distribution. The magnified image clearly shows bright spots in the wall of the pores, corresponding to single Ru atoms. The presence of Ru has been additionally confirmed by EELS (**Figure 2b**). To obtain direct information on the presence of the Ru atoms within the porous network, a typical grain of the Ru@MCM-3 was analysed by STEM-HAADF tomography. This analysis is illustrated, step by step, from the classical 2D view of the grain to its slice-by-slice 3D representation, in **Figure S6, SI**. Based on the Z contrast which is a characteristic of the STEM-HAADF images and corresponding reconstruction, the grey pixels can be assigned to the silica of MCM-41, yet the bright spots are belonging to the Ru atoms. By analysing the reconstructed volume slice-by-slice (**Figure S6, SI**), a very large amounts of white spots can be observed in the mid of the MCM-42 grains, that confirms thus the location of the Ru phase inside the grain. On an individual slice, the Ru rich areas can be directly assigned to the very contrasted white areas, while the grey ones are Ru-free and have a small contribution to the total grain. In the Ru-rich areas, the Ru distribution exhibits a roughly hexagonal structure which matches perfectly the structure of MCM-41 and, consequently, the Ru atoms are in contact with the walls of MCM-41. In contrast, the STEM-HAADF images of the Ru@MCM-1 sample show a non-uniform Ru distribution in the sample, as well as amorphous regions in the mesoporous material, which correlates with the SAXS analysis (**Figure S7, SI**).

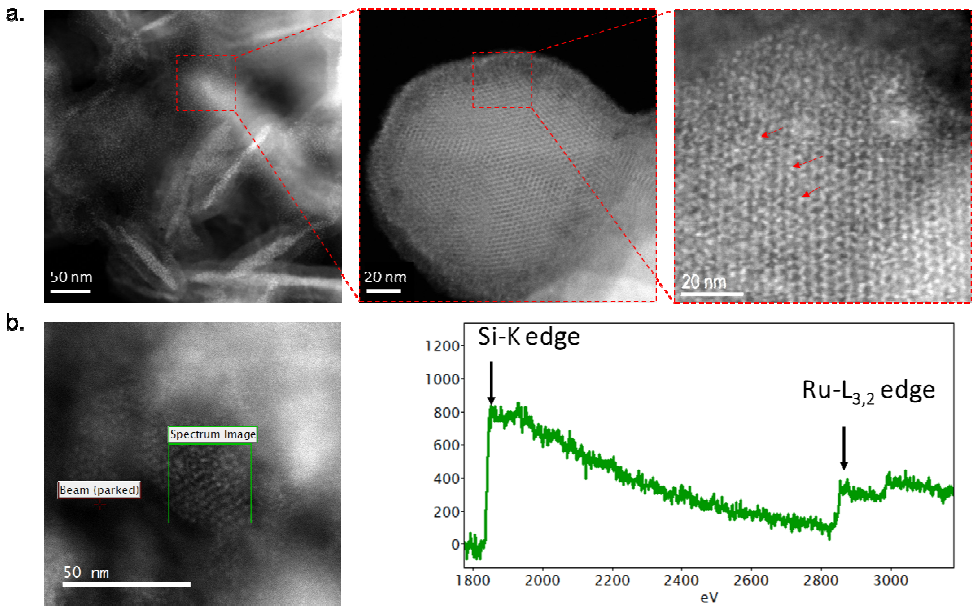

Figure 2. *STEM-HAADF image of Ru@MCM-3 sample (a) and EELS chemical analysis (b)*

The electronic state of Ru in the samples was analyzed by XPS and XAS. **Figure 3a** compares the Ru K-edge XANES spectrum of Ru@MCM-3 with reference samples. The Ru@MCM-3 spectrum exhibits a highly intense white line and is similar to that of reference RuO_2 and $Ru(OH)_3$, indicating that Ru in Ru@MCM-3 is oxidized. **Figure 3b** shows the Fourier transform (FT) EXAFS moduli of the samples (without phase shift) and **Table S1, SI** fitted distances. In agreement with the literature, [33-34] the peak at 1.95 Å is assigned to the first shell Ru-O interaction and the peak at 1.99 Å to the second shell Ru-O interaction in RuO_2 (**Table S1, SI**). Ru@MCM-3 has a spectrum similar to $Ru(OH)_3$, with a slightly longer Ru-O distance than in RuO_2. Fitting the Ru@MCM-3 EXAFS indicates that the Ru atoms are coordinated by 3.3 ± 0.5 oxygen neighbors located at 2.07 ± 0.01 Å (**Table S1, SI**).

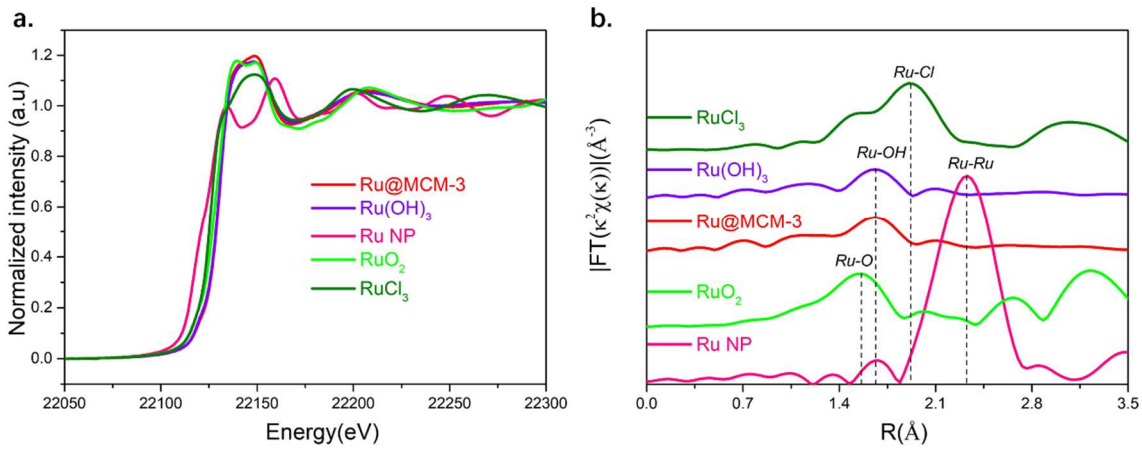

Figure 3. *Ru K-edge XANES spectra (a) and Fourier transformed χ(k)-functions of the EXAFS spectra (b) for Ru@MCM-3 and reference samples (without phase correction).*

Figure 4a shows the Ru $3p_{3/2}$ XPS spectra of metallic Ru NP, $Ru(OH)_3$ and Ru/MCM samples, and compares them with the Ru@MCM spectra. The Ru NPs and Ru/MCM spectra are characterized by a Ru $3p_{3/2}$ peak at 463.1 eV, very close to the peak of $Ru(OH)_3$, and indicating surface oxidation of the Ru particles to Ru^{3+} in Ru/MCM and in the Ru NPs [35-36]. In the Ru@MCM samples (Ru@MCM-1, Ru@MCM-3 and Ru@MCM-5), the Ru $3p_{3/2}$ peak shifts to a higher binding energy of about 463.5 eV. This could be related to the lower coordination of Ru in the Ru@MCM catalysts in the presence of CTA^+, as observed by EXAFS. Interestingly, ion exchange of CTA^+ with NH_4^+ shifts the peak to 462.3 eV. This shift suggests a partial reduction of Ru and an increase in the Ru electron density, when CTA^+ exchanges with NH_4^+. The N 1s spectra of the Ru@MCM samples with a peak at 403.4 eV (**Figure S8, SI**) are consistent with quaternary ammonium CTA^+ cations.

Ion exchange with NH_4^+ shifts this peak to 400.5 eV, characteristic for NH_4^+ ions. Thus, CTA^+ stabilizes negatively charged Ru-O species in MCM-41 structure.

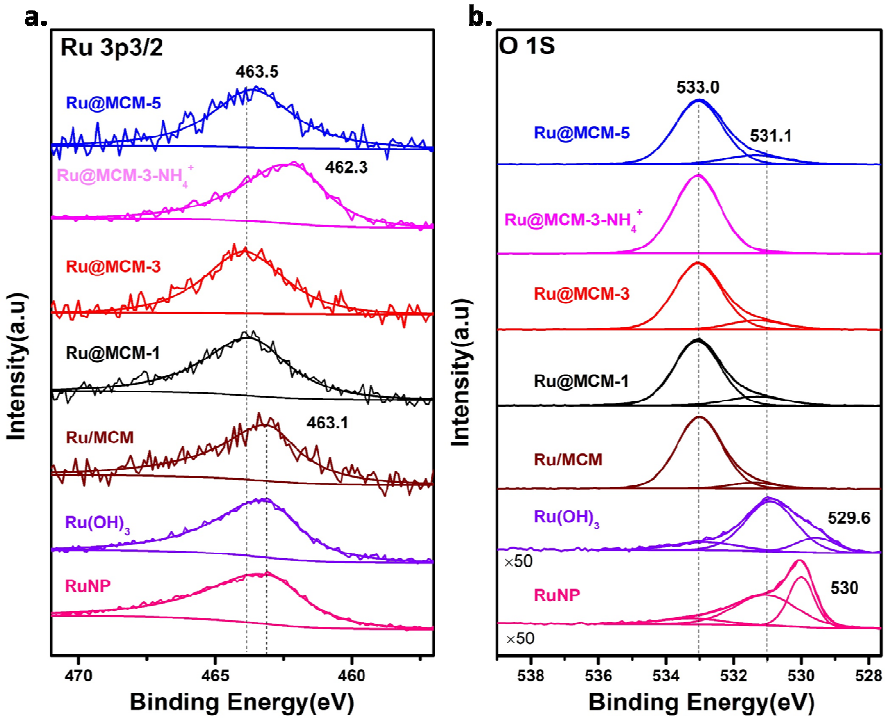

Figure 4. *XPS (a) Ru $3p_{3/2}$ and (b) O 1s core level spectra of Ru nanoparticles, Ru/MCM, $Ru(OH)_3$ and Ru@MCM samples.*

The incorporation of Ru into the MCM-41 structure during hydrolysis is further confirmed by the O 1s photoelectron spectra (**Figure 4b**). Ru NPs and $Ru(OH)_3$ have an O 1s peak at about 531 eV; this peak is associated with oxygen in Ru hydroxide. The O 1s peak at around 530 eV is associated with RuO_2[37]. All MCM-containing samples are characterized by an O 1s peak at 533.0 eV, assigned to oxygen in silica [38]. Ru/MCM, Ru@MCM-1, Ru@MCM-3, and Ru@MCM-5 have an additional small peak at 531.1 eV. This value is close to that of oxygen in $Ru(OH)_3$ and can be assigned to oxygen in the Ru-O species [39]. Previously, this peak has been observed

and attributed to Ru-O-Si species for samples with ultrathin silicon dioxide films deposited on Ru(0001) [40].

3.2 CO_2 hydrogenation activity of the Ru@MCM materials

The CO_2 hydrogenation activity of Ru@MCM was first compared with several reference catalysts under standard conditions (**Table S2, SI**) and in aqueous solution at 90 ºC. In all experiments, the same amount of Ru was loaded in the reactor (**Figure 5**). 1.3 M triethylamine (TEA) was added to increase the equilibrium conversion. Reference catalysts were prepared by deposition of Ru on carbon (Ru/C) and on MCM-41 (Ru/MCM) via impregnation followed by in situ reduction. For all the reference catalysts tested, the final formate concentrations were less than 0.1 M. Catalysts with Ru in an oxidized state ($RuCl_3$ and $Ru(OH)_3$) also show low TON and yields. In contrast, Ru@MCM-3 and Ru@MCM-5 show a TON after 15 h above 2000, reaching formate concentrations close to 1 M (**Figure 5a**) and ratio of formate to TEA about 0.7 which is close to saturation. These concentrations and TONs are comparable to those reported in the literature (**Table S2, SI**) [2-4,11-13,16,18,34-36].

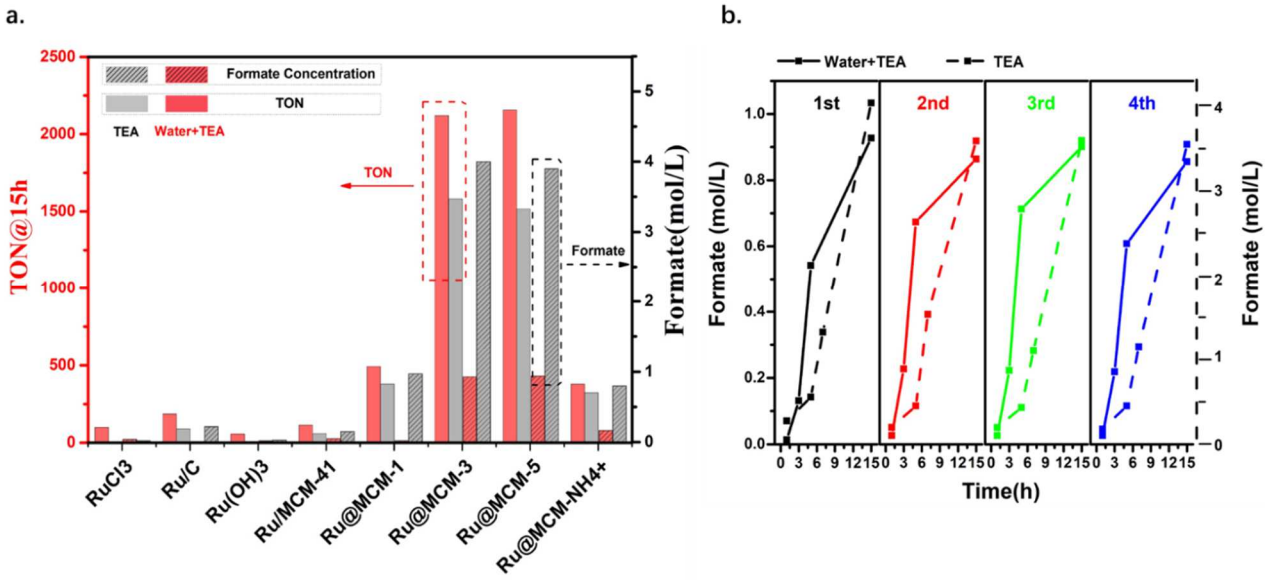

Figure 5. *a) Formate concentration and TON after 15h for CO_2 hydrogenation over a range of Ru-based catalysts; b) Demonstration of the recyclability of the Ru@MCM-3 catalyst in aqueous solution and in water-free TEA. TONs are based on the total Ru content. Reaction conditions: 0.32 mg Ru; 0.9 g TEA, 6 g water or no water, CO_2 3 MPa, H_2 2 MPa, 90 °C.*

It is interesting to note that removal of the surfactant from the pores by ion exchange with NH_4^+ significantly reduces the activity, demonstrating the importance of the quaternary ammonium surfactant for the activity of this catalyst. Investigation of the reaction conditions shows that the reaction starts at 60 °C producing formate with the 1.2 M concentration at 110 °C. The production of formate increases linearly with time (**Figure S9, SI**).

Next, the catalytic performance was evaluated in water-free conditions for the same reaction conditions. $RuCl_3$ and $Ru(OH)_3$ show negligible activity in water-free TEA. The activity of Ru/C and Ru/MCM-41 reduces by a factor two in water-free TEA reaching formate concentrations below 0.2 M after 15 h. This is likely related to the detrimental effect of strong bases on metal heterogeneous catalysts [19]. Indeed, adsorption of strong base molecule over metal surface should significantly decrease hydrogenation activity of CO_2. Also, in the presence of water CO_2 is involved in the equilibrium $CO_2/H_2CO_3/HCO_3^-$. Analysis of the catalytic activity depending on pH value demonstrated that the most favorable route proceeds through the bicarbonate HCO_3^- hydrogenation [41]. The Ru@MCM catalysts show a slight decrease (≈20 %) in the activity in water-free conditions. The formate concentrations after 15 h however

increase nearly 4-fold to 4 M for Ru@MCM-3 and Ru@MCM-5, the highest concentration reported in the literature (**Table S2, SI**). This concentration is sufficient for transfer hydrogenation reactions or for the production of concentrated formic acid by distillation [42].

Hydrogenation of CO_2 to formate over existing heterogeneous and homogeneous catalysts (**Table S2, SI**) usually requires high hydrogen and CO_2 pressures (>10 bar). The activity of Ru@MCM-3 is highly sensitive to the H_2 partial pressure both in aqueous and water-free conditions, but less sensitive to the CO_2 partial pressure, in particular for water-free TEA (**Figure 6**). It hence becomes possible to efficiently hydrogenate CO_2 at only 5 bar of CO_2 and 30 bar of H_2. This could be related to the higher CO_2 affinity of the catalyst, as seen in pulse adsorption (**Figure S10, SI**) and FTIR spectroscopy (**Figure S11, SI**). On Ru@MCM-3, CO_2 adsorption leads to the formation of carbonates by adsorption on base sites. This is similar to surfactant-containing MCM-41 (**Figure S11, SI**). The base sites are attributed to $Si\text{-}O^{-}\ldots N^{+}(CH_3)_3R$ pairs [43].

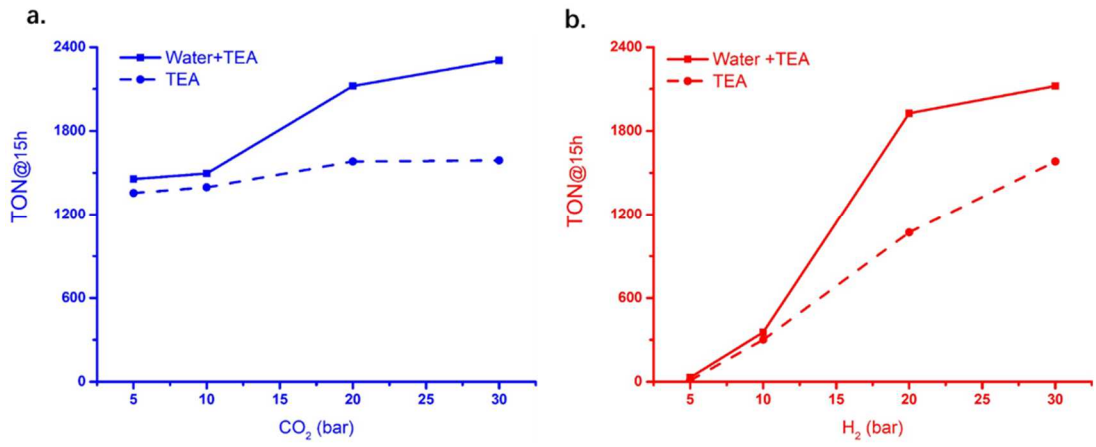

Figure 6. *Effect of H_2 and CO_2 partial pressure on the CO_2 hydrogenation activity of Ru@MCM-3. a) Fixed H_2 pressure at 30 bar, b) Fixed CO_2 pressure at 20 bar.*

Reaction conditions: aqueous solution (10 mg catalyst, 0.9 g TEA, 6 g water, 90 °C, reaction time: 15 h) and pure TEA (10 mg catalyst, 0.9 g TEA, 90 °C, reaction time: 15 h)

Existing heterogeneous catalysts for CO_2 hydrogenation to formate typically irreversibly deactivate by the strong adsorption of the base co-reactant [44]. In contrast, **Figure 5b** shows that Ru@MCM-3 can be recycled without loss in activity for aqueous and water-free reactions. Characterization after reaction shows no loss in Ru or CTA^+ (**Table 1** and **Figure S2, SI**) and no change in the electronic state of Ru (**Figure S12, SI** and **Table S1, SI**). Note that under similar conditions, the CTA^+ surfactant leaches from MCM-41 (**Figure S13, SI**), yet, the surfactant is retained in the pores of Ru@MCM-3. This suggests that the Ru species in the walls of the MCM structure strongly interact with the CTA^+ surfactant, thereby enhancing the stability of the surfactant inside the pores of Ru@MCM-3. The surfactant blocks adsorption during low-temperature N_2 adsorption (**Table 1**), which could be due to the transformation of micelles to semicrystalline state according to the literature [45]. At the same time, in the liquid phase under the reaction conditions, the surfactant allows high solubility and diffusion of gases in micelles [46]. Thus, the surfactant allows efficient transport of CO_2 and H_2 toward the Ru active sites with subsequent removal of formate product through the hydrophilic interface of MCM-41 and surfactant.

3.3 DFT modelling

To gain insight into the unique reactivity of Ru@MCM-3 for the hydrogenation of CO_2 to formate, density functional theory (DFT) calculations were performed using the cluster model depicted in **Figure 7a** and **Figure S14, SI**. Liu and Feher showed that silsesquioxane cages sufficiently reproduce the relative stability of the metal center and the silica ring strain for such single metal sites in MCM-41, and that structural and electronic effects of the active site are dominated by the local structure [47]. EXAFS data showed that the Ru centers are coordinated by 3 to 4 O atoms in the solid phase (see **Table S1, SI**). In our cluster model, Ru has three bonds with the MCM-41 framework.

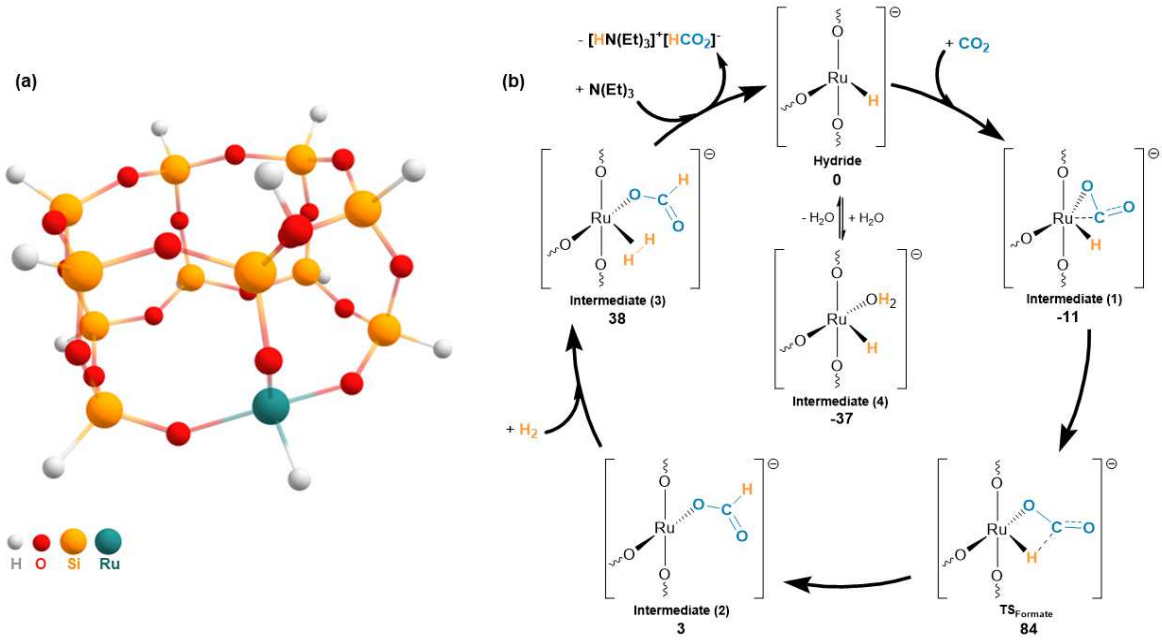

Figure 7. *(a) Silesquioxane cage of the Ru-Hydride active site; (b) Catalytic cycle and respective Gibbs free energies (kJ.mol^{-1}) for the proposed mechanism for Ru@MCM-3. DFT calculations performed with PBE0/TZP//PBE0/SVP at 298 K.*

We first evaluated the adsorption of water on this Ru^{3+} center (**Figure 8**). On this open site model, the adsorption of water is favorable and the 6-coordinated structure

with 2 water molecules **C** is 16 kJ/mol more stable than the less-coordinated structure **A**. These calculations indicate that adsorption of water can inhibit the activity of the catalysts. Also, adsorption of water on the Ru-H species, deactivates the catalyst (Intermediate (4), **Figure 7b**). The same effect could be during adsorption of TEA. We hypothesize that the hydrophobic and bulky nature of the template limits the concentration of water and TEA near the Ru sites, and most of the Ru^{3+} centers in Ru@MCM-3 are therefore present as the low coordinated species **A**, while the hexacoordinated species **C** would be preferred, once the template is removed. A feature of Ru@MCM-3 is the presence of the surfactant (CTA^+) in the pores of the catalyst; removing the surfactant reduces the activity of the catalyst (see **Figure 5**). The size of the surfactant correlates to the hydrophobicity of the pores, the longer the aliphatic chain of the template, the more hydrophobic the inside of the pore will be. Additionally, CTA^+ behaves as a counter-ion in the ion pair (CTA^+)(OSi-O^-), thus stabilizing basic sites in the pores, which should repel basic TEA molecule from Ru [48]. Previous studies on the effect of the surfactant length on the basicity of Si-MCM-41 materials have shown that voluminous cations lead to weaker interactions between the ion pair, thus increasing the basicity of the site[48].

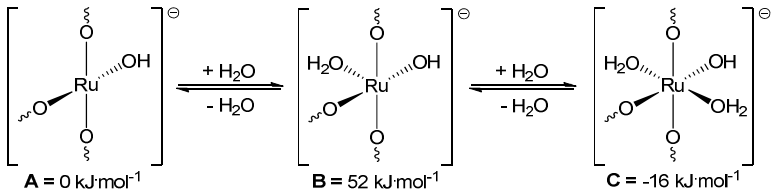

Figure 8. *Relative stability of 4-, 5- and 6- coordinated Ru species in the Ru@MCM-3 cluster model. DFT calculations performed with PBE0/TZP//PBE0/SVP at 298 K.*

It was previously established that hydrogen dissociated heterolytically on single-atom catalysts with no change in the formal oxidation state of the metal center [49]. Once the catalytic active species, the Ru-H, is formed, the reaction follows 4 steps: CO_2 addition resulting in Intermediate (1), formate synthesis yielding Intermediate (2), hydrogen activation producing Intermediate (3), and release of the formate with the aid of a strong base with concurrent regeneration of the active species. The simplified catalytic cycle and the respective free energies are shown in **Figure 7b** (see also Figure **S15, SI**). The heterolytic dissociation of hydrogen to form the hydride from Intermediate (3) can happen with a variety of bases (OH^-, O_3SiO^-, HCO_2^-, HCO_3^-) or with the aid of $N(Et)_3$.

With formate as the base, this reaction has a barrier of 88 $kJ \cdot mol^{-1}$, and the corresponding transition state is the highest point along the free energy profile (**Table S3, SI** and **Figure S16, SI**), while the reaction is essentially barrierless with the stronger base $N(Et)_3$ (**Figure S17, SI**). Since the proton transfer depends critically on the local environment and on the proximity of the base, we did not explicitly include this step in **Figure 7b**.

4. Conclusion

A new class of single-site Ru heterogeneous catalysts is reported. The Ru single atoms are incorporated in the walls of MCM-41 and stabilized by CTA^+ as surfactant. This catalyst efficiently hydrogenates CO_2 to formate under mild conditions in

water-free conditions, reaching formate concentrations of 4 M. DFT modelling suggests that heterolytic hydrogen activation and hydride transfer to CO_2 over low-coordinated Ru(III) species are the key steps in the mechanism and that the CTA^+ surfactant stabilizes the Ru species in a low-coordinated state.

Acknowledgments

Qiyan Wang thanks the ANR Nano4FUT project for stipend for PhD research. Sara Santos, César A. Urbina-Blanco and Mark Saeys acknowledge the support from VLAIO with the cluster SBO project CO2PERATE (project number HBC.2017.0692) and from UGent High-Performance Computing (HPC). The computational resources (Stevin Supercomputer Infrastructure) and services used in this work were provided by the VSC (Flemish Supercomputer Center), funded by Ghent University, FWO and the Flemish Government – department EWI. César A. Urbina-Blanco acknowledges financial support from a senior postdoctoral fellowship from the Fund for Scientific Research Flanders (FWO). We thank the Swiss Light Source for providing beamtime at the SuperXAS beamline.

Additional information

Supplementary Information is available for this this paper

Competing interests: The authors declare no competing interests.

References

[1] J. Dou, Y. Sheng, C. Choong, L. Chen, H.C. Zeng, Silica nanowires encapsulated Ru nanoparticles as stable nanocatalysts for selective hydrogenation of CO_2 to CO, Applied Catalysis B: Environmental, 219 (2017) 580-591, https://doi.org/10.1016/j.apcatb.2020.119384.

[2] A. Alvarez, A. Bansode, A. Urakawa, A.V. Bavykina, T.A. Wezendonk, M. Makkee, J. Gascon, F. Kapteijn, Challenges in the Greener Production of Formates/Formic Acid, Methanol, and DME by Heterogeneously Catalyzed CO_2 Hydrogenation Processes, Chem Rev, 117 (2017) 9804-9838, https://doi.org/10.1021/acs.chemrev.6b00816.

[3] K. Mori, T. Sano, H. Kobayashi, H. Yamashita, Surface Engineering of a Supported PdAg Catalyst for Hydrogenation of CO_2 to Formic Acid: Elucidating the Active Pd Atoms in Alloy Nanoparticles, Journal of the American Chemical Society, 140 (2018) 8902-8909, https://doi.org/10.1021/jacs.8b04852.

[4] Z. Chen, T. Fan, Y.-Q. Zhang, J. Xiao, M. Gao, N. Duan, J. Zhang, J. Li, Q. Liu, X. Yi, Wavy SnO_2 catalyzed simultaneous reinforcement of carbon dioxide adsorption and activation towards electrochemical conversion of CO_2 to HCOOH, Applied Catalysis B: Environmental, 261 (2020) 118243, https://doi.org/10.1016/j.apcatb.2019.118243.

[5] J.T. Gray, S.W. Kang, J.-I. Yang, N. Kruse, J.-S. McEwen, J.C. Park, S. Ha, Unravelling the reaction mechanism of gas-phase formic acid decomposition on highly dispersed Mo_2C nanoparticles supported on graphene flakes, Applied Catalysis B: Environmental, 264 (2020) 118478, https://doi.org/10.1016/j.apcatb.2019.118478.

[6] J. Klankermayer, S. Wesselbaum, K. Beydoun, W. Leitner, Selective Catalytic Synthesis Using the Combination of Carbon Dioxide and Hydrogen: Catalytic Chess at the Interface of Energy and Chemistry, Angew Chem Int Ed Engl, 55 (2016) 7296-7343, https://doi.org/10.1002/anie.201507458.

[7] C. Vogt, M. Monai, G.J. Kramer, B.M. Weckhuysen, The renaissance of the Sabatier reaction and its applications on Earth and in space, Nature Catalysis, 2 (2019) 188-197, https://doi.org/10.1038/s41929-019-0244-4.

[8] F. Chen, P. Zhang, Y. Zeng, R. Kosol, L. Xiao, X. Feng, J. Li, G. Liu, J. Wu, G. Yang, Vapor-phase low-temperature methanol synthesis from CO_2-containing syngas via self-catalysis of methanol and Cu/ZnO catalysts prepared by solid-state method, Applied Catalysis B: Environmental, 279 (2020) 119382, https://doi.org/10.1016/j.apcatb.2020.119382.

[9] Z. Li, Q. Xu, Metal-Nanoparticle-Catalyzed Hydrogen Generation from Formic Acid, Acc Chem Res, 50 (2017) 1449-1458, https://doi.org/10.1021/acs.accounts.7b00132.

[10] Y. Chen, H. Li, W. Zhao, W. Zhang, J. Li, W. Li, X. Zheng, W. Yan, W. Zhang, J. Zhu, R. Si, J. Zeng, Optimizing reaction paths for methanol synthesis from CO_2 hydrogenation via metal-ligand cooperativity, Nat Commun, 10 (2019) 1885, https://doi.org/10.1038/s41467-019-09918-z.

[11] J. Kothandaraman, A. Goeppert, M. Czaun, G.A. Olah, G.K. Prakash, Conversion of CO_2 from Air into Methanol Using a Polyamine and a Homogeneous Ruthenium Catalyst, Journal of the American Chemical Society, 138 (2016) 778-781, https://doi.org/10.1021/jacs.5b12354.

[12] C.L. Mathis, J. Geary, Y. Ardon, M.S. Reese, M.A. Philliber, R.T. VanderLinden, C.T. Saouma, Thermodynamic Analysis of Metal–Ligand Cooperativity of PNP Ru Complexes: Implications for CO_2 Hydrogenation to Methanol and Catalyst Inhibition, Journal of the American Chemical Society, 141 (2019) 14317-14328, https://doi.org/10.1021/jacs.9b06760.

[13] S.K. Lee, M. Kondo, M. Okamura, T. Enomoto, G. Nakamura, S. Masaoka, Function-Integrated Ru Catalyst for Photochemical CO_2 Reduction, Journal of the American Chemical Society, 140 (2018) 16899-16903, https://doi.org/10.1021/jacs.8b09933.

[14] D.A. Bulushev, J.R.H. Ross, Heterogeneous catalysts for hydrogenation of CO_2 and bicarbonates to formic acid and formates, Catalysis Reviews, 60 (2018) 566-593, https://doi.org/10.1080/01614940.2018.1476806.

[15] P. Kuhn, M. Antonietti, A. Thomas, Porous, covalent triazine ‐ based frameworks prepared by ionothermal synthesis, Angewandte Chemie International Edition, 47 (2008) 3450-3453, https://doi.org/10.1002/anie.200705710.

[16] K. Rohmann, J. Kothe, M.W. Haenel, U. Englert, M. Hölscher, W. Leitner, Hydrogenation of CO_2 to formic acid with a highly active ruthenium acriphos complex in DMSO and DMSO/water, Angewandte Chemie International Edition, 55 (2016) 8966-8969, https://doi.org/10.1002/anie.201603878.

[17] S. Wesselbaum, V. Moha, M. Meuresch, S. Brosinski, K.M. Thenert, J. Kothe, T. vom Stein, U. Englert, M. Hölscher, J. Klankermayer, Hydrogenation of carbon dioxide to methanol using a homogeneous ruthenium-Triphos catalyst: from mechanistic investigations to multiphase catalysis, Chemical science, 6 (2015) 693-704, https://doi.org/10.1039/c4sc02087a.

[18] C.A. Huff, M.S. Sanford, Catalytic CO_2 Hydrogenation to Formate by a Ruthenium Pincer Complex, ACS Catalysis, 3 (2013) 2412-2416, https://doi.org/10.1021/cs400609u.

[19] Z. Jin, X. Wang, S. Wang, D. Li, G. Lu, The effect of triethylamine on the hydrodechlorination of chlorophenols on Pd/C at low temperature, Catalysis Communications, 10 (2009) 2027-2030, https://doi.org/10.1016/j.catcom.2009.07.024.

[20] T. Schaub, D.M. Fries, R. Paciello, K.-D. Mohl, M. Schäfer, S. Rittinger, D. Schneider, Process for preparing formic acid by reaction of carbon dioxide with hydrogen, U.S. Patent (2014), NO. 8,791,297.

[21] J.D. Leonard, Preparation of formic acid by hydrolysis of methyl formate, U.S. Patent (1981), NO. 4,299,981.

[22] X. Lv, W. Wei, H. Wang, B. Huang, Y. Dai, Holey graphitic carbon nitride (g-CN) supported bifunctional single atom electrocatalysts for highly efficient overall water splitting, Applied Catalysis B: Environmental, 264 (2020) 118521, https://doi.org/10.1016/j.apcatb.2019.118521.

[23] B. Qiao, A. Wang, X. Yang, L.F. Allard, Z. Jiang, Y. Cui, J. Liu, J. Li, T. Zhang, Single-atom catalysis of CO oxidation using Pt_1/FeO_x, Nat Chem, 3 (2011) 634-641, https://doi.org/10.1038/nchem.1095.

[24] J. Liu, Catalysis by supported single metal atoms, Acs Catalysis, 7 (2017) 34-59, https://doi.org/10.1021/acscatal.6b01534.

[25] X. Zhou, L. Chen, G.E. Sterbinsky, D. Mukherjee, R.R. Unocic, S.L. Tait, Pt-Ligand single-atom catalysts: tuning activity by oxide support defect density, Catalysis Science & Technology, 10 (2020) 3353-3365, https://doi.org/10.1039/C9CY02594D.

[26] H. Yan, S. Yao, B. Yin, W. Liang, X. Jin, X. Feng, Y. Liu, X. Chen, C. Yang, Synergistic effects of bimetallic PtRu/MCM-41 nanocatalysts for glycerol oxidation in base-free medium: Structure and electronic coupling dependent activity, Applied Catalysis B: Environmental, 259 (2019) 118070, https://doi.org/10.1016/j.apcatb.2019.118070.

[27] S. Lyu, Q. Cheng, Y. Liu, Y. Tian, T. Ding, Z. Jiang, J. Zhang, F. Gao, L. Dong, J. Bao, Dopamine sacrificial coating strategy driving formation of highly active surface-exposed Ru sites on Ru/TiO_2 catalysts in Fischer–Tropsch synthesis, Applied Catalysis B: Environmental, 278 (2020) 119261, https://doi.org/10.1016/j.apcatb.2020.119261.

[28] J. Ilavsky, Nika: software for two-dimensional data reduction, Journal of Applied Crystallography, 45 (2012) 324-328, https://doi.org/10.1107/S0021889812004037.

[29] B. Ravel, M. Newville, ATHENA, ARTEMIS, HEPHAESTUS: data analysis for X-ray absorption spectroscopy using IFEFFIT, J Synchrotron Radiat, 12 (2005) 537-541, https://doi.org/10.1107/S0909049505012719.

[30] Y. Feng, W. Li, M. Meng, H. Yin, J. Mi, Mesoporous Sn (IV) doping MCM-41 supported Pd nanoparticles for enhanced selective catalytic oxidation of 1, 2-propanediol to pyruvic acid, Applied Catalysis B: Environmental, 253 (2019) 111-120, https://doi.org/10.1016/j.apcatb.2019.04.051.

[31] J. Dou, Y. Sheng, C. Choong, L. Chen, H.C. Zeng, Silica nanowires encapsulated Ru nanoparticles as stable nanocatalysts for selective hydrogenation of CO_2 to CO, Applied Catalysis B: Environmental, 219 (2017) 580-591, https://doi.org/10.1016/j.apcatb.2017.07.083.

[32] T. Dwars, E. Paetzold, G. Oehme, Reactions in micellar systems, Angew Chem Int Ed Engl, 44 (2005) 7174-7199, https://doi.org/10.1002/anie.200501365.

[33] J. Yu, A. Wang, W. Yu, X. Liu, X. Li, H. Liu, Y. Hu, Y. Wu, W. Zhou, Tailoring the ruthenium reactive sites on N doped molybdenum carbide nanosheets via the anti-Ostwald ripening as efficient electrocatalyst for hydrogen evolution reaction in alkaline media, Applied Catalysis B: Environmental, 277 (2020) 119236, https://doi.org/10.1016/j.apcatb.2020.119236.

[34] S. Tian, Z. Wang, W. Gong, W. Chen, Q. Feng, Q. Xu, C. Chen, C. Chen, Q. Peng, L. Gu, H. Zhao, P. Hu, D. Wang, Y. Li, Temperature-Controlled Selectivity of Hydrogenation and Hydrodeoxygenation in the Conversion of Biomass Molecule by the Ru_1/mpg-C_3N_4 Catalyst, Journal of the American Chemical Society, 140 (2018) 11161-11164, https://doi.org/10.1021/jacs.8b06029.

[35] G. Liang, Y. Zhou, J. Zhao, A.Y. Khodakov, V.V. Ordomsky, Structure-Sensitive and Insensitive Reactions in Alcohol Amination over Nonsupported Ru Nanoparticles, ACS Catalysis, 8 (2018) 11226-11234, https://doi.org/10.1021/acscatal.8b02866.

[36] D. Zagoraios, C. Panaritis, A. Krassakopoulou, E.A. Baranova, A. Katsaounis, C.G. Vayenas, Electrochemical Promotion of Ru Nanoparticles deposited on a Proton Conductor Electrolyte during CO_2 Hydrogenation, Applied Catalysis B: Environmental, (2020) 119148, https://doi.org/10.1016/j.apcatb.2020.119148.

[37] A.M. Abdel-Mageed, K. Wiese, M. Parlinska-Wojtan, J. Rabeah, A. Brückner, R.J. Behm, Encapsulation of Ru nanoparticles: Modifying the reactivity toward CO and CO_2 methanation on highly active Ru/TiO_2 catalysts, Applied Catalysis B: Environmental, (2020) 118846, https://doi.org/10.1016/j.apcatb.2020.118846.

[38] J. Chastain, R.C. King Jr, Handbook of X-ray photoelectron spectroscopy, Perkin-Elmer Corporation, 40 (1992) 221.

[39] K. Mori, T. Taga, H. Yamashita, Isolated Single-Atomic Ru Catalyst Bound on a Layered Double Hydroxide for Hydrogenation of CO_2 to Formic Acid, ACS Catalysis, 7 (2017) 3147-3151, https://doi.org/10.1021/acscatal.7b00312.

[40] A.G. Y. B. He, C. Korte,A. Farkas,G. Mellau,P. Dudin, L. Gregoratti, A. Barinov, M. Kiskinova,A. Stierle, N. Kasper,S. Bajt, and H. Over, Oxidation and Reduction of Ultrathin Nanocrystalline Ru Films on Silicon: Model System for Ru-Capped Extreme Ultraviolet Lithography Optics, J. Phys. Chem. C, 111 (2007) 10988-10992, https://doi.org/10.1021/jp071339b.

[41] G. Laurenczy, F. Joó, L. Nádasdi, Formation and characterization of water-soluble hydrido-ruthenium (II) complexes of 1, 3, 5-triaza-7-phosphaadamantane and their catalytic activity in hydrogenation of CO_2 and HCO_3-in aqueous solution, Inorganic chemistry, 39 (2000) 5083-5088, https://doi.org/10.1021/ic000200b.

[42] H. Brunner, W. Leitner, Enantioselective Catalytic Transfer-Hydrogenation of α-Unsaturated Carboxylic Acids with Triethylammonium Formate, Angewandte Chemie International Edition in English, 27 (1988) 1180-1181, https://doi.org/10.1002/anie.198811801.

[43] S. Zribi, B. Albela, L. Bonneviot, M.S. Zina, Surface engineering and palladium dispersion in MCM-41 for methane oxidation, Applied Catalysis A: General, 502 (2015) 195-203, https://doi.org/10.1016/j.apcata.2015.06.015.

[44] Q. Liu, X. Yang, L. Li, S. Miao, Y. Li, Y. Li, X. Wang, Y. Huang, T. Zhang, Direct catalytic hydrogenation of CO_2 to formate over a Schiff-base-mediated gold nanocatalyst, Nat Commun, 8 (2017) 1407, https://doi.org/10.1038/s41467-017-01673-3.

[45] A.M. Mihut, M. Drechsler, M. Möller, M. Ballauff, Sphere-to-rod transition of micelles formed by the semicrystalline polybutadiene-block-poly (ethylene oxide) block copolymer in a selective solvent, Macromolecular rapid communications, 31 (2010) 449-453, https://doi.org/10.1002/marc.200900571.

[46] J. Zhang, B. Han, J. Li, Y. Zhao, G. Yang, Carbon dioxide in ionic liquid microemulsions, Angewandte Chemie International Edition, 50 (2011) 9911-9915, https://doi.org/10.1002/ange.201103956.

[47] C. Liu, J. Camacho-Bunquin, M. Ferrandon, A. Savara, H. Sohn, D. Yang, D.M. Kaphan, R.R. Langeslay, P.A. Ignacio-de Leon, S. Liu, U. Das, B. Yang, A.S. Hock, P.C. Stair, L.A. Curtiss, M. Delferro, Development of activity–descriptor relationships for supported metal ion hydrogenation catalysts on silica, Polyhedron, 152 (2018) 73-83, https://doi.org/10.1016/j.poly.2018.06.006.

[48] C.I.A. Alegre, M.F. Zalazar, B. Bulhões Cazula, H.J. Alves, N.M. Peruchena, Molecular Insights on the Role of (CTA^+)(SiO^-) Ion Pair into the Catalytic Activity of [CTA^+]–Si–MCM-41, Topics in Catalysis, 62 (2019) 941-955, https://doi.org/10.1007/s11244-019-01181-2.

[49] I.V. Yentekakis, G. Goula, M. Hatzisymeon, I. Betsi-Argyropoulou, G. Botzolaki, K. Kousi, D.I. Kondarides, M.J. Taylor, C.M. Parlett, A. Osatiashtiani, Effect of support oxygen storage capacity on the catalytic performance of Rh nanoparticles for CO_2 reforming of methane, Applied Catalysis B: Environmental, 243 (2019) 490-501, https://doi.org/10.1016/j.apcatb.2018.10.048.

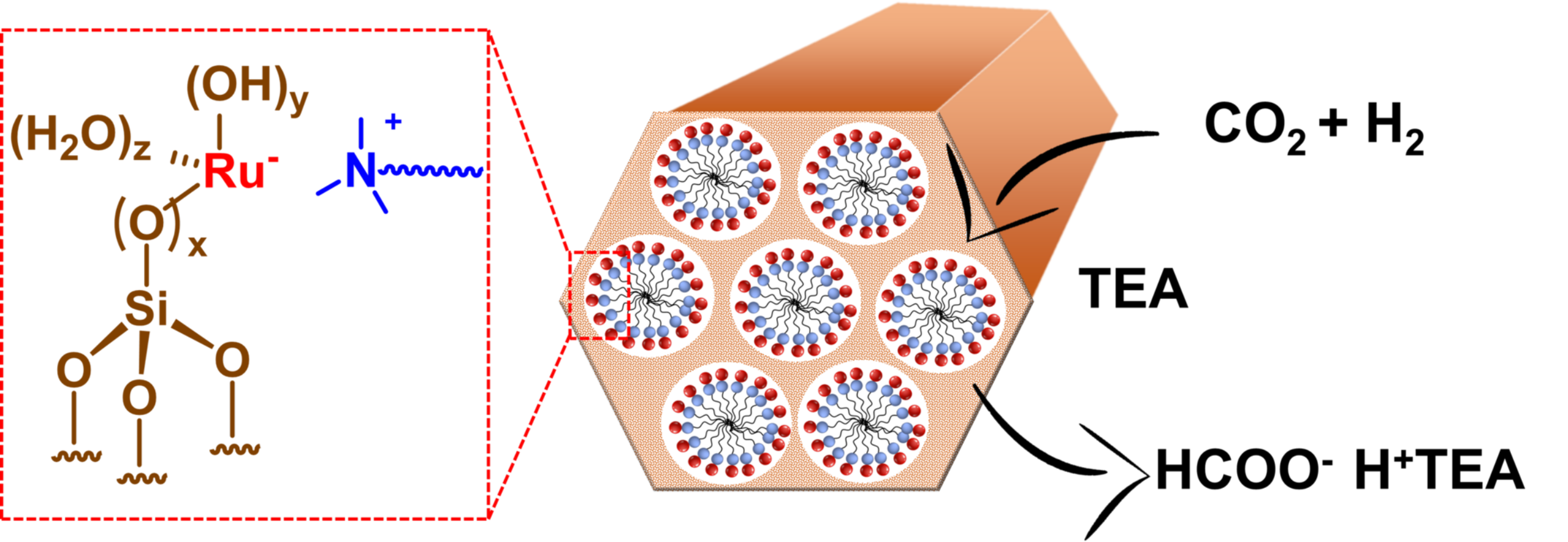
(OH)y
(H2O)z
Ru-
(O)x
Si
O
O
O
N+
CO2 + H2
TEA
HCOO- H+TEA